Folding of Prestin's Anion-Binding Site and the Mechanism of Outer Hair Cell Electromotility

Xiaoxuan Lin[1], Patrick Haller[1,2], Navid Bavi[1,2], Nabil Faruk[1], Eduardo Perozo[1,2,3,4,*], Tobin R. Sosnick[1,4,5,*]

[1]Department of Biochemistry and Molecular Biology, [2]Center for Mechanical Excitability, [3]Institute for Neuroscience, [4]Institute for Biophysical Dynamics, [5]Prizker School for Molecular Engineering, The University of Chicago, Chicago, Illinois, USA

*Corresponding authors: trsosnic@uchicago.edu; eperozo@uchicago.edu.

Abstract

Prestin (SLC26A5) responds to transmembrane voltage fluctuations by changing its cross-sectional area, a process underlying the electromotility of outer hair cells and cochlear amplification. Prestin's voltage-dependent conformational rearrangements partially depend on the binding of Cl^- to an electrostatic gap between the TM3 and TM10 helices. Using hydrogen-deuterium exchange mass spectrometry, we find that prestin displays an unstable anion-binding site, where folding of the amino termini of TM3 and TM10 is coupled to Cl^- binding. This event shortens the TM3-TM10 electrostatic gap, thereby reducing prestin's cross-sectional area. These folding events upon anion-binding are absent in SLC26A9, an anion transporter closely related to prestin. We observe helix fraying of prestin's anion-binding site but cooperative unfolding of multiple peripheral helices, with implications to prestin's fast electromechanical rearrangements. These results highlight a novel role of the folding equilibrium of the anion-binding site in defining prestin's unique voltage-sensing mechanism and electromotility.

Introduction

Hearing sensitivity in mammals is sharply tuned by a cochlear amplifier associated with electromotile length changes in outer hair cells[1]. These changes are driven by prestin (SLC26A5), a member of the SLC26 anion transporter family, which converts voltage-dependent conformational transitions into cross-sectional area changes, affecting its footprint in the lipid bilayer[2]. This process plays a major role in mammalian cochlear amplification and frequency selectivity, with prestin knockout producing a 40-60 dB signal loss in live cochleae[3]. Unlike most molecular motors, where force is exerted from chemical energy transduction, prestin behaves as a putative piezoelectric device, where mechanical and electrical transduction are coupled[4]. As a result, prestin functions as a direct voltage-to-force transducer. Prestin's piezoelectric properties are unique among members of the SLC26 family, where most of the SLC26 homologs function as anion transporters.

Recent structures determined by cryo-electron microscopy (cryo-EM) have sampled prestin's conformational space under various anionic environments and located the anion-binding site at the electrostatic gap between the amino-termini of TM3 and TM10 helices[5–7]. This partially hydrophobic anion-binding pocket is influenced by surrounding residues in TM1 and by a fixed positive charge from residue R399 on TM10. Movements of this binding site are coupled to the complex reorientation of the core domain relative to the gate domain[5,6], reminiscent of the conformational transitions in transporters displaying an elevator-like mechanism[8]. Prestin exhibits minimal transporter ability yet is structurally similar to the non-electromotive anion transporter SLC26A9 (sequence identity = 34%; Cα RMSD = 3.4 Å for the transmembrane domain (TMD), PDB: 7S8X and 6RTC)[7,9,10]. Questions remain as to the molecular basis underlying the distinct functions of the two proteins. Importantly, the role of bound anions, which is required for prestin electromotility[11], is still elusive.

Prestin's voltage dependence is tightly regulated by intracellular anions of varying valence and structure[12,13], whereas anion affinity is also regulated by voltage and tension[14]. These phenomena suggest that anions, rather than behaving as explicit gating charges, may serve as allosteric modulators[14]. Incorporating a fixed charge alternative to a bound anion through an S398E mutation preserves prestin's nonlinear capacitance (NLC) but results in insensitivity to salicylate, a strong competing anionic binder[7]. Except for residue R399 near the anion-binding site, charged residues located in the TMD distribute towards the membrane-water interface[5–7] and display minimal contributions to the total gating charge estimated from NLCs[15]. Electrostatic calculations show that R399 has a strong contribution to the local electrostatics at the anion-binding site, by providing ~40% of the positive charge at the bilayer mid-plane[5]. However, to understand prestin's voltage dependence on both negative[11] and positive (R399[5,16]) charges in relatively close proximity, one will require a further understanding of local electrostatics and overall dynamics at the anion-binding site.

Here we studied the influence of anion-binding on the dynamics and structure of prestin as a function of anions (Cl^-, SO_4^{2-}, salicylate, and Hepes) via hydrogen-deuterium exchange mass spectrometry (HDX-MS). The Hepes condition was achieved by Cl^- removal (dialysis), which inhibits prestin's NLC[11], and hence induced an apo state. We assumed a low affinity of Hepes anions due to their large size. Furthermore, prestin's NLC shifts to depolarized potentials in a Hepes-based buffer, suggesting that at 0 mV, prestin adopts a more expanded state that is coupled to low anion affinity[12,13]. By comparing the dynamics of prestin with its close non-piezoelectric relative, the anion transporter SLC26A9, we identified

distinct features unique to prestin, including a relatively unstable anion-binding site that folds upon binding, thereby allosterically modulating the dynamics of the TMD. In contrast, the stability and hydrogen-bond pattern of SLC26A9's anion-binding site were minimally affected by anion binding. We observed fraying of the helices involved in the binding site whereas cooperative unfolding of multiple peripheral helices, which may explain prestin's fast and large-scale motions. These results highlight the significance of the anion-binding site's folding equilibrium in understanding the unique properties of prestin's voltage dependence and electromotility.

Results

We carried out HDX measurements on dolphin prestin and mouse SLC26A9 solubilized in glyco-diosgenin (GDN) at either pD_{read} 7.1, 25 °C or pD_{read} 6.1, 0 °C (**Table S1**). These conditions provided an effective labeling time window spanning seven log units, allowing us to determine HDX rates and protection factors (PFs) throughout the protein[17]. Under our experimental conditions, the observed HDX rates report on the stability, as exchange occurs mostly via EX2 kinetics (**Supplementary Text**). The HDX data are presented in terms of the relevant region with the specific sequence and peptide noted in parentheses (**Methods**), e.g., the N-terminus of prestin's TM10 ($Region_{394–397}$: $Peptide_{392–397}$). Although we mostly focused on the anion-binding site, we obtained thermodynamic information throughout the two proteins that complements the recent cryo-EM structures[5–7] (**Supplementary Text**).

<u>Prestin's anion-binding site is less stable than SLC26A9's.</u>

To examine the effect of anion binding to the dynamics of prestin and SLC26A9, we dialyzed the proteins purified in Cl^- into a Hepes buffer lacking other anions. Cl^- removal resulted in distinct stability changes for prestin and SLC26A9, manifested by significant HDX acceleration for prestin while mild HDX slowing for SLC26A9 (**Fig. 1 & Fig. S1**). These HDX effects indicate that anion binding induced global stabilization for prestin while slight destabilization for SLC26A9 (**Fig. 1**).

Among the observed HDX responses for prestin, the HDX acceleration at the anion-binding pocket appeared to be the most pronounced and indicate local stabilization induced by anion binding (**Fig. 2A**). In detail, HDX accelerated by 20-fold for the N-termini of both TM3 ($Region_{136-142}$: $Peptide_{134-142}$ + 9 other peptides) and TM10 ($Region_{394–397}$: $Peptide_{392–397}$) (**Fig. 2A & Fig. S9.22-9.31**). This HDX change translates to a difference in free energy of unfolding (ΔΔG) by at least 1.8 kcal/mol; $\Delta\Delta G^{\text{binding site}}_{\text{Cl-apo}}$ = 1.8 kcal/mol. At least four residues in the middle of TM1 exhibited faster HDX ($Region_{90-101}$: $Peptide_{88-101}$ + 10 other peptides), collectively by 350-fold; $\Delta\Delta G^{\text{TM1}}_{\text{Cl-apo}}$ = 3.5 kcal/mol (**Fig. 1A & Fig. S9.6-9.16**). The TM1 region with accelerated HDX included L93, Q97, and F101, residues that are known to participate in the binding pocket[5,6,18].

SLC26A9 exhibited similar stability as prestin in Cl^- for the majority of the TMD, except for the N-terminal TM3 ($Region_{131-134}$: $Peptide_{129-134}$) which exchanged at least 100-fold slower than that of prestin's ($Region_{136-142}$: $Peptide_{134-142}$) (**Fig. 2**). This difference in HDX points to a relatively unstable anion-binding site of prestin as compared to SLC26A9; $\Delta\Delta G^{\text{N-terminal TM3}}_{\text{SLC26A9-prestin}}$ > 2.8 kcal/mol, and was also seen in the site-resolved PFs that were obtained by deconvoluting the HDX-MS data using PyHDX[19] (**Fig. S2**).

Compared to the 20~350-fold HDX acceleration observed at prestin's binding site upon Cl^- removal, HDX of SLC26A9's binding pocket was only affected mildly (**Fig. 2B**). These included a slight slowing in HDX for the N-termini of TM3 ($Region_{131-134}$: $Peptide_{129-134}$) and TM10 ($Region_{392-395}$: $Peptide_{390-395}$) (**Fig. 2B**). The TM1 ($Region_{72-92}$: $Peptide_{83-92}$ + 10 other peptides) continued to remain undeuterated even after 27 h (**Fig. 2B & Fig. S10.4-10.14**), emphasizing the intrinsic high stability of SLC26A9's anion-binding pocket.

In addition to the binding pocket, we observed stability changes in various regions of the TMDs for prestin and SLC26A9 that reflect their distinct functions. For prestin, anion binding resulted in stabilization for the intracellular cavity but destabilization for regions facing the extracellular matrix (**Fig. 1C & Fig. S1A**). The stabilizing effects for the cytosol-facing regions were manifested by HDX acceleration upon Cl^- removal at the linker between TM2 and TM3, and the intracellular portions of TM7, TM8, & TM9 ($Region_{128-135}$, $Region_{284-294}$, & $Region_{354-375}$) (**Fig. S9.22-9.27, S9.58-9.64, S9.82-9.87**). In contrast, HDX slowed for the regions facing the extracellular environment, namely the extracellular ends of TM5b, TM6, and TM7 ($Region_{250-262}$ & $Region_{309-316}$) (**Fig. S9.45-9.51, S9.66-9.68, S9.71**). However, for SLC26A9, anion binding destabilized the cytosol-facing regions, as HDX slowed by ~5-fold upon Cl^- removal for the intracellular ends of TM8, TM9, and TM12 ($Region_{351-369}$ & $Region_{440-455}$) (**Fig. 1C, Fig. S1B, & Fig. S10.62-10.63, S10.77-10.82**). The distinct thermodynamic

consequences of anion binding for prestin and SLC26A9 are reflective of their distinct functions as a motor and a transporter, respectively.

Anion binding drives the folding of prestin's binding site.

In the apo state of prestin, the 20-fold HDX acceleration for the binding site (**Fig. 2A**) is consistent with a process of local destabilization, even unfolding, or increased solvent accessibility as the region becomes exposed to the intracellular water cavity[5]. To investigate these possibilities, we measured prestin's HDX in response to a chaotrope, urea, which destabilizes proteins by interacting with backbone amides[20]. In a background of 360 mM Cl^-, the addition of 4 M urea accelerated HDX for the N-terminus of TM3 ($Region_{137\text{-}140}$: $Peptide_{134\text{-}140}$) by 20-fold (**Fig. 3A**), suggesting that this region was destabilized and accessible to urea in its exchange-competent state. In apo prestin, however, the PF at the N-terminus of TM3 was unaffected by urea (after accounting for the known ~50% slowing of the intrinsic exchange rate[20], k_{chem}) (**Fig. 3A**), arguing that this region was already unfolded prior to the addition of urea[21].

We note that in apparent contradiction to our inference that the N-terminus of TM3 was unfolded in the apo state, its HDX was ~100-fold slower than k_{chem}. Such apparent PF for an unfolded region has been reported when it is located inside an outer membrane β-barrel, rationalized by the region having a lower effective local concentration of the HDX catalyst, [OD^-], than in bulk solvent[22,23]. For prestin, we propose that detergent molecules in the micelle can restrict the access of OD^- to amide protons and thus produce the apparent PF for the unfolded N-terminus of TM3.

The folding reversibility of the anion-binding site was evaluated by tracking the HDX for 5 min after titrating in Cl^- to apo prestin. Deuteration levels for the N-terminus of TM3 ($Region_{137\text{-}140}$) decreased with increasing Cl^- concentration (**Fig. 3B**), suggesting reversible folding upon Cl^- binding. Similar behavior was seen in the middle of TM1 ($Region_{86\text{-}101}$: $Peptide_{84\text{-}101}$) as Cl^- binding stabilized the binding pocket (**Fig. 3B**).

Cryo-EM structures of prestin in Cl^-, SO_4^{2-}, and salicylate likely have sampled the conformations during its areal expansion cycle by shifting the voltage dependence of the NLC towards depolarized potentials[5,6]. When SO_4^{2-} is the major anion, prestin's HDX was nearly identical as in Cl^-, except for a slightly faster HDX at the anion-binding site ($Region_{128\text{-}142}$ and $Region_{394\text{–}397}$) at labeling times longer than 10^3 s (**Fig. 4**). This mild HDX response suggested a slightly destabilized binding site while the remaining regions retained normal dynamics as in Cl^-. In the presence of salicylate, HDX slowed across the TMD, with the greatest effect seen at the anion-binding site (10-fold; $\Delta\Delta G^{\text{binding site}}_{\text{salicylate-Cl-}}$ = 1.4 kcal/mol) (**Fig. 4**), indicating that salicylate binding to prestin globally stabilized the TMD, primarily at the anion-binding site. These stability changes are in agreement with the cryo-EM structural analysis[5].

Incremental unfolding of prestin's binding site versus cooperative unfolding of the peripheral helices.

Our broad HDX time range and dense sampling allowed us to observe effects at the residue level. In particular, the binding site of prestin ($Region_{128\text{-}140}$ and $Region_{394\text{–}397}$) exhibited a broad deuterium uptake curve in Cl^-, indicative of helix fraying where exchange of deuterium occurs from multiple states that differ by one hydrogen bond (**Fig. 5A**). Such HDX pattern is consistent with the associated residues undergoing sequential unfolding with distinct PFs (i.e., stability). Site-resolved PFs obtained using PyHDX[19] support that the stability increased residue-by-residue for TM3 for amide protons located further away from the substrate (**Fig. S3A**). This gradual increase in residue stability along the helices is indicative of helix fraying starting from prestin's binding site.

In contrast, we observed much more cooperative unfolding in prestin's peripheral helices, with exchange occurring from one or a few high energy states where a set of hydrogen bonds are broken concertedly. Cooperatively exchanging residues have similar PFs and a characteristic sigmoidal deuterium uptake curve for the associated peptide, as seen in prestin's intracellular portion of TM6 ($Region_{275\text{-}282}$: $Peptide_{273\text{-}282}$ + 4 peptides) (**Fig. 5A & Fig. S9.53-9.57**).

To characterize the degree of cooperativity for the HDX at the N-terminus of TM3 ($Peptide_{134\text{-}140}$) and the intracellular portion of TM6 ($Peptide_{273\text{-}282}$), we fit the deuterium uptake curves as a sum of exponentials[17], $D(t) = \sum_{i=1}^{n}(1 - e^{-k_i t})$, where k_i is the exchange rate and n is the number of exponentials, ranging from one to the number of exchange-competent residues. The value of n was determined by the quality of the fit, evaluated by χ^2 and having a relative error smaller than one (i.e., standard deviation for k_i less than k_i itself). HDX data for the N-terminus of prestin's TM3 ($Peptide_{134\text{-}140}$) was fit with four well-separated exponentials with rates spanning five log units for the four residues (**Fig. 5A**). The need to individually fit each site indicates a lack of cooperativity and helix fraying. In contrast, the peptide

representing the intracellular portion of TM6 ($Peptide_{273-282}$) has eight residues yet it could be fitted with only three rates spanning less than two log units (**Fig. 5A**). This rather concerted deuterium uptake was independent of the anion substrate identity and also observed for TM1, TM5b, the intracellular portion of TM7, and the N-terminus of TM8 (**Fig. S9.6-9.16, S9.42-9.43, S9.45-9.51, S9.58-9.63, S9.78-9.79**).

We define a parameter $\sigma_{\Delta G}$ to quantify the degree of folding cooperativity. The value of $\sigma_{\Delta G}$ is calculated as the standard deviation for the free energies of unfolding (ΔGs) for exchange-competent residues comprising the peptide. When a region folds 100% cooperatively, $\sigma_{\Delta G}$ is zero as all residues have the same ΔG. As the diversity increases (lower cooperativity), the $\sigma_{\Delta G}$ value becomes larger. The accuracy of the ΔG determination at residue level can be increased by comparing uptake curves for overlapping peptides and/or deconvoluting isotope envelopes[17]. Here we assigned exchange rates (k_i), obtained from the fitting method mentioned above, to residues based on the directionality of helix fraying, with residues closer to the end of a helix having faster rates. When there is ambiguity on which rate to assign to a given residue, the geometric mean of the rates was used (**Methods**). We found that prestin's intracellular portion of TM6 ($Peptide_{273-282}$) has $\sigma_{\Delta G}$ = 1.1, indicating mild cooperativity, whereas the non-cooperative N-terminal TM3 ($Peptide_{134-140}$) has a $\sigma_{\Delta G}$ = 2.9. This significant decrease in folding cooperativity for helices directly involved in the Cl^- binding site likely has functional consequences related to prestin's electromotility.

Discussion

Using HDX-MS, we have explored the energetic and conformational differences between prestin, a voltage-dependent motor that underlies the electromotility of outer hair cells, and its close relative SLC26A9, a representative member of the SLC26 family of anion transporters. This comparison addresses underlying mechanistic questions related to the unique properties of prestin, the origin of its voltage dependence, and the potential mechanisms that couple charge movements to electromotility. Despite the structural similarities between the two proteins, our data point to major differences in the energetics at the anion-binding site (**Fig. S2**). Prestin displays an unstable binding site that, upon Cl^- unbinding, unfolds by one helical turn at the electrostatic gap formed by the abutting (antiparallel) short helices TM3 and TM10 (**Fig. 2A & Fig. 3**). We measured an increase in local ΔΔG = 1.8~3.5 kcal/mol upon anion binding. This energy difference is within the range of the ΔΔG = 2.4 kcal/mol estimated from having a 60-fold excess of Cl^- above the EC_{50} (6 mM)[11]. Similar folding events upon anion binding are absent in SLC26A9 (**Fig. 2B**), pointing to a key role of the bound anion as a structural element in prestin, stabilizing the natural repulsion between TM3-TM10 positive helical macrodipoles. This phenomenon rationalizes the conundrum that prestin's voltage dependence requires the proximity of a bound anion to R399.

We find that anion binding to prestin mainly stabilizes the interface between the scaffold and the elevator domains (**Fig. 1C & Fig. S1A**). This phenomenon is consistent with an elevator-like mechanism during prestin's conformational transition from the expanded to the contracted state[5]. Anion binding stabilizes prestin's intracellular cavity and slightly destabilizes regions facing the extracellular matrix. This effect can result from changes in solvent exposure, as the intracellular water cavity may shrink as prestin contracts. For SLC26A9, the destabilization upon anion binding at the intracellular cavity likely results from a shift from the outward-facing state to the inward-facing state (**Fig. 1C & Fig. S1B**), supporting the alternate-access mechanism for this fast transporter[9,10]. Similar HDX changes, i.e., increased HDX on the intracellular side while slowed HDX on the extracellular side, have been observed in other transporters during their transition from outward-facing to inward-facing states[24,25]. Prestin's distinct HDX response compared to canonical transporters is consistent with it being an incomplete anion transporter[11,26].

The HDX data for prestin in Cl^-, SO_4^{2-}, and salicylate support an allosteric role for the anion binding at the TM3-TM10 electrostatic gap[12–14] (**Fig. 4**). SO_4^{2-} binding leads to shifts in the NLC towards positive potentials, thus stabilizing multiple conformations that are on average more expanded than prestin in Cl^- [5,13,27]. Since the binding of SO_4^{2-} to prestin is weaker than that of Cl^- [6], the slight increase in HDX at the binding site likely reflects more prestin molecules adopting the apo state. Salicylate binding inhibits prestin's NLC and yet the molecular basis of such inhibition remains obscure[5,16]. Bavi *et al*[5] showed that binding of salicylate occludes prestin's binding pocket from solvent and inhibits the movement of TM3 and TM10. This is fully consistent with the 10-fold HDX slowing found for the N-termini of TM3 and TM10 upon

salicylate binding as compared to the rest of the protein. Our HDX data, together with results from Bavi *et al.*[5], suggest that salicylate likely inhibits prestin's NLC by restricting the dynamics of the anion-binding site.

We identified helix fraying at the anion-binding site of prestin based on its broad deuterium uptake curve in the presence of Cl^-, consistent with a multi-state landscape (**Fig. 5A**). This fraying suggests that an increase in the anion concentration would promote helical propensity at TM3 and TM10, and is inconsistent with a cooperative (two-state) model involving an equilibrium between an apo state and a single bound state (**Fig. 5A**). Therefore, we suggest that a two-state model of prestin's conformational changes with a high energy barrier would be insufficient to explain its fast kinetics, whereas charge movement is facilitated by crossing multiple shallow barriers[13,28].

We propose that having a Cl^- binding site that frays can promote prestin's fast motor response which is thought to have evolved independently of its voltage sensing ability[29,30]. While prestin's TM3 and TM10 have similar stability, SLC26A9 exhibits a non-fraying TM3 that is more stable than TM10 (**Fig. 2**). Furthermore, the normally highly conserved Pro136 in mammalian prestin is replaced with a Threonine in other vertebrates that express non-electromotile prestin (**Fig. S4A**). This Pro136Thr substitution, based on our Upside MD simulations, results in a hyper-stabilized TM3 that would otherwise have similar folding stability as TM10 (**Fig. S4B**). A Pro136Thr mutation in rat prestin also leads to a shift of NLC towards depolarized potentials[18]. These thermodynamic and functional consequences of having a destabilized TM3 with Pro136, which now has similar stability as TM10, lead us to hypothesize that prestin's fast somatic motility may be promoted by having simultaneous fraying of the TM3 and TM10 helices.

Helices that exhibit cooperative unfolding largely match helices showing conformational rearrangements in the cryo-EM structures[5]. These helices all appear to be peripheral (lipid-facing) helices, including TM6-TM7, TM1, TM5b, and TM8. The region with the most pronounced cooperativity, the intracellular portion of TM6, has a series of glycines including the consecutive G274-G275 pair that underlies the "electromotility elbow", a helical bending contributing to the largest cross-sectional area (expanded conformation) and the thin notch in the micelle[5]. The structural consequences of cooperativity speak to the significance of these helices in prestin's area expansion. We propose that cooperativity allows for long-range allostery[31] so that the lipid-facing helices can adopt large-scale structural rearrangements as induced by voltage sensor movements, thereby achieving rapid electromechanical conversions of prestin. The exact mechanism through which cooperativity contributes to prestin's electromotility remains a key question.

Based on the structural and allosteric role of Cl^- binding at the TM3-TM10 electrostatic gap, we propose a model in which prestin's conformational changes and electromotility are regulated by the folding equilibrium of the anion-binding site (**Fig. 5B**). In our model, anion binding participates in a local electrostatic balance that includes the positively charged R399 and the positive TM3-TM10 helical macrodipoles. In the apo state, the anion-binding site unfolds due to the electrostatic repulsion between these positively charged groups. Being a buried charge, R399 may exit from the electric field concentrated in the lower dielectric environment of the protein, and move into the solvent region as it lacks a neutralizing anion. This event is coupled to the allosteric expansion of prestin's membrane footprint[5]. Anion binding partially neutralizes the positive electric field at the binding site, an event that is coupled to the residue-by-residue folding for the N-termini of TM3 and TM10 as well as the shortening of the electrostatic gap. This folding event results in a more focused electric field and consequent contraction of prestin's intermembrane cross-sectional area. At physiologically-relevant low Cl^- concentration (1.5-4 mM)[32], prestin's binding site is likely to be only partially folded. Complete folding may be achieved by membrane potential acting on the TM3-TM10 helical dipoles, which leads to the movement of the voltage sensor across the electric field and the rapid areal expansion for the TMDs (i.e., electromotility).

Conclusions

We applied HDX-MS to the study of prestin's electromotility within the framework of extensive structural data. HDX was able to identify folding events that are likely critical for function but had escaped detection by cryo-EM. The folding equilibrium of the Cl^- binding site and its dependence on Cl^- concentration appears to rationalize the conundrum of how an anion that binds in proximity to a positive charge (R399), can enable the NLC of prestin. We observed fraying of the helices forming the anion-binding site, which contrasts with cooperative unfolding of the peripheral helices. We believe that the non-cooperative fraying of the helices involved in voltage sensing may allow for fast charge movements within

the electric field. This heightened sensitivity of the voltage sensor then induces large-scale motions of the peripheral helices, enabled by their cooperativity (or allostery), thereby altering the cross-sectional area of prestin. These principles warrant further investigation.

Methods

Sample preparation for prestin and SLC26A9. Generation of the dolphin prestin and mouse SLC26A9 constructs, protein overexpression, and purification were conducted using the same protocol as previously described[5]. Following the cleavage of the GFP tag, the protein was purified by size-exclusion chromatography on a Superose 6, 10/300 GE column (GE Healthcare), with the running buffer being either the "Cl^-/H_2O Buffer" or the "SO_4^{2-}/H_2O Buffer", including 1 µg/ml aprotinin and 1 µg/ml pepstatin[5]. The "Cl^-/H_2O Buffer" contained 360 mM NaCl, 20 mM Tris, 3 mM dithiothreitol, 1 mM EDTA, and 0.02% GDN at pH 7.5. The "SO_4^{2-}/H_2O Buffer" contained 140 mM Na_2SO_4, 5 mM $MgSO_4$, 20 mM Tris, 0.02% GDN, and 10-15 mM methanesulfonic acid to adjust the pH to 7.5. Peak fractions containing the sample were concentrated on a 100K MWCO centrifugal filter (Millipore) to 2-3 mg/mL, flash-frozen in liquid nitrogen, and kept at −80 °C until use.

Hydrogen-deuterium exchange. HDX reactions, quench, and injection were all performed manually. Prior to HDX, proteins purified in Cl^- and SO_4^{2-} were buffer exchanged to the same H_2O buffer without protease inhibitor using 7K MWCO Zeba spin desalting columns (Thermo 89882). For HDX conducted in Hepes, proteins purified in Cl^- were dialyzed against the "Hepes/H_2O Buffer" (150 mM Hepes, 0.02% GDN, pH adjusted to 7.5 by Hepes acid or base) using a 10K MWCO dialysis device (Thermo Slide-A-Lyzer MINI 69570) with three times of buffer exchange for near-complete Cl^- removal. HDX in a solution of 93% deuterium (D) content was initiated by diluting 2 µL of 25 µM prestin or SLC26A9 stock in an H_2O buffer into 28 µL of the corresponding buffer made with D_2O (99.9% D, Sigma-Aldrich 151882). HDX was conducted in one of the two conditions: 1) pD_{read} 7.1, 25 °C; 2) pD_{read} 6.1, 0 °C. The D_2O buffers contained the same compositions as the corresponding H_2O buffers, except that Tris was replaced with Phosphate for the "SO_4^{2-}/D_2O Buffer" for both HDX conditions, and the "Cl^-/D_2O Buffer" for HDX performed at pD_{read} 6.1, 0 °C. The pD_{read} was adjusted to 7.1 or 6.1 by DCl for the "Cl^-/D_2O Buffers" and by NaOD for other D_2O buffers. For HDX in the presence of salicylate, 50 mM salicylate acid was added to the "SO_4^{2-}/D_2O Buffer" and the pD_{read} was adjusted by NaOD. For HDX in the presence of urea, 4 M urea was added to the "Cl^-/D_2O Buffer" or the "Hepes/D_2O Buffer", with accurate urea concentration determined to be 4.16 M and 4.54 M, respectively, by refractive index using a refractometer (WAY Abbe)[33]. HDX was quenched at various times, ranging from 1 s to 27 h, by the addition of 30 µL of ice-chilled quench buffer containing 600 mM Glycine, 8 M urea, pH 2.5. For HDX in the presence of urea, urea concentration in the quench buffer was adjusted to reach a 4 M final concentration. Quenched reactions were immediately injected into a valve system maintained at 5 °C (Trajan LEAP). Non-deuterated controls and MS/MS runs for peptide assignment were performed with the same protocol as above except D_2O buffers were replaced by H_2O buffers, followed by the immediate addition of the quench buffer and injection. HDX reactions were performed in random order. No peptide carryover was observed as accessed by following sample runs with injections of quench buffer containing 4 M urea and 0.01% GDN. In-exchange controls accounting for forward deuteration towards 41.5% D in the quenched reaction were performed by mixing D_2O buffer and ice-chilled quench buffer prior to the addition of the protein. Maximally labeled controls ("All D") accounting for back-exchange were performed by a 48-h incubation with the "Cl^-/D_2O Buffer" at 37 °C, followed by a 30-min incubation with 8 M of deuterated urea at 25 °C.

Protease digestion and LC-MS. Upon injection, the protein was digested online by a pepsin/FPXIII (Sigma-Aldrich P6887/P2143) mixed protease column maintained at 20 °C. Protease columns were prepared in-house by coupling the protease to a resin (Thermo Scientific POROS 20 Al aldehyde activated resin 1602906) and hand-packing into a column (2 mm ID × 2 cm, IDEX C-130B). After digestion, peptides were desalted by flowing across a hand-packed trap column (Thermo Scientific POROS R2 reversed-phase resin 1112906, 1 mm ID × 2 cm, IDEX C-128) at 5 °C. The total time for digestion and desalting was 2.5 min at 100 µL/min of 0.1% formic acid at pH 2.5. Peptides were then separated on a C18 analytical column (TARGA, Higgins Analytical, TS-05M5-C183, 50 x 0.5 mm, 3 µm particle size) via a 14-min, 10–60% (vol/vol) acetonitrile (0.1% formic acid) gradient applied by a Dionex UltiMate-3000 pump. Eluted peptides were analyzed

by a Thermo Q Exactive mass spectrometer. MS data collection, peptide assignments by SearchGUI version 4.0.25, and HDX data processing by HDExaminer 3.1 (Sierra Analytics) were performed as previously described[22,23].

HDX data presentation, correction, quantification, and statistics. In our labeling convention, we name capitalized regions according to the third residue of each peptide since the first two residues have much faster k_{chem}[34,35] and hence, exhibit complete back-exchange. Labeling times for HDX performed in pD_{read} 6.1, 0 °C were corrected to those in pD_{read} 7.1, 25 °C by a factor of 140, determined by the ratio of the k_{chem} for full-length proteins in the two conditions – prestin: $\tau_{chem}^{\mathrm{pDread\ 6.1,0\ °C}}$ = 10 sec, $\tau_{chem}^{\mathrm{pDread\ 7.1,25\ °C}}$ = 74 msec; SLC26A9: $\tau_{chem}^{\mathrm{pDread\ 6.1,0\ °C}}$ = 9 sec, $\tau_{chem}^{\mathrm{pDread\ 7.1,25\ °C}}$ = 65 msec. Deuteration levels were adjusted with the 93% D content but not with back-exchange levels except for **Fig. 5A**. For HDX in the presence of urea (**Fig. 3A**), D contents of 76% and 74% were used to account for the volumes of 4.16 M and 4.54 M urea in the "Cl^-/D_2O Buffer" and the "Hepes/D_2O Buffer", respectively.

HDX rates, protection factors (PFs), and changes of free energy of unfolding (ΔΔG's) in the Results section were estimated by fitting uptake curves of each peptide, after correcting for back-exchange levels, with a stretched exponential as described by Hamuro 2021[17], except for discussion relevant to **Fig. 5A**. Peptides with less than 10% D at the longest labeling time (~10^5 s) were not used for fitting. The residue-level ΔΔG values presented in the full-length proteins in **Fig. 1C** were estimated by averaging ΔΔG values for peptides containing the residue. We note that this stretched exponential method is only a rough approximation to extract ΔΔG's and our major conclusions are not dependent on this fitting method.

For fitting HDX data and extracting rates relevant to **Fig. 5A**, HDX data were first normalized to in- and back-exchange levels. Given the helices are likely to exchange by fraying, the exchange rate for each residue was assigned based on their distance from the end of the helix. When a residue could not be assigned to a single rate, the geometric mean of the possible rates was used, e.g., the HDX data for the 8-residue $Peptide_{273\text{-}282}$ were well fit with 3 exponentials, and the three associated rates, k_1, k_2, & k_3, were assigned to the 8 residues according to k_1, k_1, $(k_1k_1k_2)^{1/3}$, k_2, k_2, $(k_2k_2k_3)^{1/3}$, k_3, & k_3. These rates were used to calculate folding stability according to $\Delta G = -RT\ln(k_{chem}/k_i - 1)$.

A hybrid statistical analysis used to generate **Fig. S1** was performed as described by Hageman & Weis, 2019[36], with significance limits defined at α = 0.05. **Table S1** provides biochemical and statistical details for HDX in this study.

MD simulations. Missing residues for prestin (PDB 7S8X) were built using MODELLER[37] and the placement within the bilayers was accomplished using Positioning of Proteins in Membranes webserver[38]. Simulations were conducted in our Upside molecular dynamics package[39,40] using a membrane thickness of 38 Å. Local restraints in the form of small springs between nearby residues were used to maintain the native structure of cytosolic domains, as well as to the TM13-TM14 helices. Also, the distance between the two TMDs was held fixed. We ran 28 temperature replicas between 318 and 360K.

Acknowledgments

This work was supported by grants to T.R.S. from the NSF (MCB 2023077) and the NIH (GM55694, 1R35GM148233), and to E.P. from R01 DC019833.

Reference

1. Dallos, P., Zheng, J. & Cheatham, M. A. Prestin and the cochlear amplifier. *J. Physiol.* **576**, 37–42 (2006).
2. Sfondouris, J., Rajagopalan, L., Pereira, F. A. & Brownell, W. E. Membrane Composition Modulates Prestin-associated Charge Movement. *J. Biol. Chem.* **283**, 22473–22481 (2008).
3. Liberman, M. C. *et al.* Prestin is required for electromotility of the outer hair cell and for the cochlear amplifier. *Nature* **419**, 5 (2002).

4. Dong, X., Ospeck, M. & Iwasa, K. H. Piezoelectric Reciprocal Relationship of the Membrane Motor in the Cochlear Outer Hair Cell. *Biophys. J.* **82**, 1254–1259 (2002).
5. Bavi, N. *et al.* The conformational cycle of prestin underlies outer-hair cell electromotility. *Nature* **600**, 553–558 (2021).
6. Ge, J. *et al.* Molecular mechanism of prestin electromotive signal amplification. *Cell* **184**, 4669-4679.e13 (2021).
7. Butan, C. *et al.* Single particle cryo-EM structure of the outer hair cell motor protein prestin. *Nat. Commun.* 40 (2022).
8. Garaeva, A. A. & Slotboom, D. J. Elevator-type mechanisms of membrane transport. *Biochem. Soc. Trans.* **48**, 1227–1241 (2020).
9. Walter, J. D., Sawicka, M. & Dutzler, R. Cryo-EM structures and functional characterization of murine Slc26a9 reveal mechanism of uncoupled chloride transport. *eLife* **8**, e46986 (2019).
10. Chi, X. *et al.* Structural insights into the gating mechanism of human SLC26A9 mediated by its C-terminal sequence. *Cell Discov.* **6**, 55 (2020).
11. Oliver, D. *et al.* Intracellular Anions as the Voltage Sensor of Prestin, the Outer Hair Cell Motor Protein. *Science* **292**, 2340–2343 (2001).
12. Rybalchenko, V. & Santos-Sacchi, J. Cl− flux through a non-selective, stretch-sensitive conductance influences the outer hair cell motor of the guinea-pig. *J. Physiol.* **547**, 873–891 (2003).
13. Rybalchenko, V. & Santos-Sacchi, J. Anion Control of Voltage Sensing by the Motor Protein Prestin in Outer Hair Cells. *Biophys. J.* **95**, 4439–4447 (2008).
14. Song, L. & Santos-Sacchi, J. Conformational State-Dependent Anion Binding in Prestin: Evidence for Allosteric Modulation. *Biophys. J.* **98**, 371–376 (2010).
15. Bai, J.-P. *et al.* Prestin's Anion Transport and Voltage-Sensing Capabilities Are Independent. *Biophys. J.* **96**, 3179–3186 (2009).
16. Gorbunov, D. *et al.* Molecular architecture and the structural basis for anion interaction in prestin and SLC26 transporters. *Nat. Commun.* **5**, 3622 (2014).
17. Hamuro, Y. Quantitative Hydrogen/Deuterium Exchange Mass Spectrometry. *J. Am. Soc. Mass Spectrom.* **32**, 2711–2727 (2021).
18. Schaechinger, T. J. *et al.* A synthetic prestin reveals protein domains and molecular operation of outer hair cell piezoelectricity. *EMBO J.* **30**, 2793–2804 (2011).
19. Smit, J. H. *et al.* Probing Universal Protein Dynamics Using Hydrogen–Deuterium Exchange Mass Spectrometry-Derived Residue-Level Gibbs Free Energy. *Anal. Chem.* **93**, 12840–12847 (2021).
20. Lim, W. K., Rösgen, J. & Englander, S. W. Urea, but not guanidinium, destabilizes proteins by forming hydrogen bonds to the peptide group. *Proc. Natl. Acad. Sci.* **106**, 2595–2600 (2009).
21. Ramesh, R. *et al.* Uncovering metastability and disassembly hotspots in whole viral particles. *Prog. Biophys. Mol. Biol.* **143**, 5–12 (2019).
22. Zmyslowski, A. M., Baxa, M. C., Gagnon, I. A. & Sosnick, T. R. HDX-MS performed on BtuB in E. coli outer membranes delineates the luminal domain's allostery and unfolding upon B12 and TonB binding. *Proc. Natl. Acad. Sci.* **119**, e2119436119 (2022).
23. Lin, X., Zmyslowski, A. M., Gagnon, I. A., Nakamoto, R. K. & Sosnick, T. R. Development of in vivo HDX-MS with applications to a TonB-dependent transporter and other proteins. *Protein Sci.* **31**, e4402 (2022).
24. Merkle, P. S. *et al.* Substrate-modulated unwinding of transmembrane helices in the NSS transporter LeuT. *Sci. Adv.* **4**, eaar6179 (2018).
25. Martens, C. *et al.* Direct protein-lipid interactions shape the conformational landscape of secondary transporters. *Nat. Commun.* **9**, 4151 (2018).
26. Schaechinger, T. J. & Oliver, D. Nonmammalian orthologs of prestin (SLC26A5) are electrogenic divalent/chloride anion exchangers. *Proc. Natl. Acad. Sci.* **104**, 7693–7698 (2007).
27. Muallem, D. & Ashmore, J. An Anion Antiporter Model of Prestin, the Outer Hair Cell Motor Protein. *Biophys. J.* **90**, 4035–4045 (2006).
28. Santos-Sacchi, J., Navarrete, E. & Song, L. Fast Electromechanical Amplification in the Lateral Membrane of the Outer Hair Cell. *Biophys. J.* **96**, 739–747 (2009).
29. Tan, X. *et al.* A motif of eleven amino acids is a structural adaptation that facilitates motor capability of eutherian prestin. *J. Cell Sci.* **125**, 1039–1047 (2012).

30. Tang, J., Pecka, J. L., Fritzsch, B., Beisel, K. W. & He, D. Z. Z. Lizard and Frog Prestin: Evolutionary Insight into Functional Changes. *PLoS ONE* **8**, e54388 (2013).
31. Hilser, V. J. & Thompson, E. B. Intrinsic disorder as a mechanism to optimize allosteric coupling in proteins. *Proc. Natl. Acad. Sci.* **104**, 8311–8315 (2007).
32. McPherson, D. R. Sensory Hair Cells: An Introduction to Structure and Physiology. *Integr. Comp. Biol.* **58**, 282–300 (2018).
33. Warren, J. R. & Gordon, J. A. On the Refractive Indices of Aqueous Solutions of Urea. *J. Phys. Chem.* **70**, 297–300 (1966).
34. Bai, Y., Milne, J. S., Mayne, L. & Englander, S. W. Primary Structure Effects on Peptide Group Hydrogen Exchange. *Proteins* **17**, 75–86 (1993).
35. Nguyen, D., Mayne, L., Phillips, M. C. & Englander, S. W. Reference parameters for protein hydrogen exchange rates. *J. Am. Soc. Mass Spectrom.* **29**, 1936–1939 (2018).
36. Hageman, T. S. & Weis, D. D. Reliable Identification of Significant Differences in Differential Hydrogen Exchange-Mass Spectrometry Measurements Using a Hybrid Significance Testing Approach. *Anal. Chem.* **91**, 8008–8016 (2019).
37. Sali, A. & Blundell, T. L. Comparative protein modelling by satisfaction of spatial restraints. *J. Mol. Biol.* **234**, 779–815 (1993).
38. Lomize, A. L., Todd, S. C. & Pogozheva, I. D. Spatial arrangement of proteins in planar and curved membranes by PPM 3.0. *Protein Sci. Publ. Protein Soc.* **31**, 209–220 (2022).
39. Jumper, J. M., Faruk, N. F., Freed, K. F. & Sosnick, T. R. Accurate calculation of side chain packing and free energy with applications to protein molecular dynamics. *PLOS Comput. Biol.* **14**, e1006342 (2018).
40. Jumper, J. M., Faruk, N. F., Freed, K. F. & Sosnick, T. R. Trajectory-based training enables protein simulations with accurate folding and Boltzmann ensembles in cpu-hours. *PLOS Comput. Biol.* **14**, e1006578 (2018).

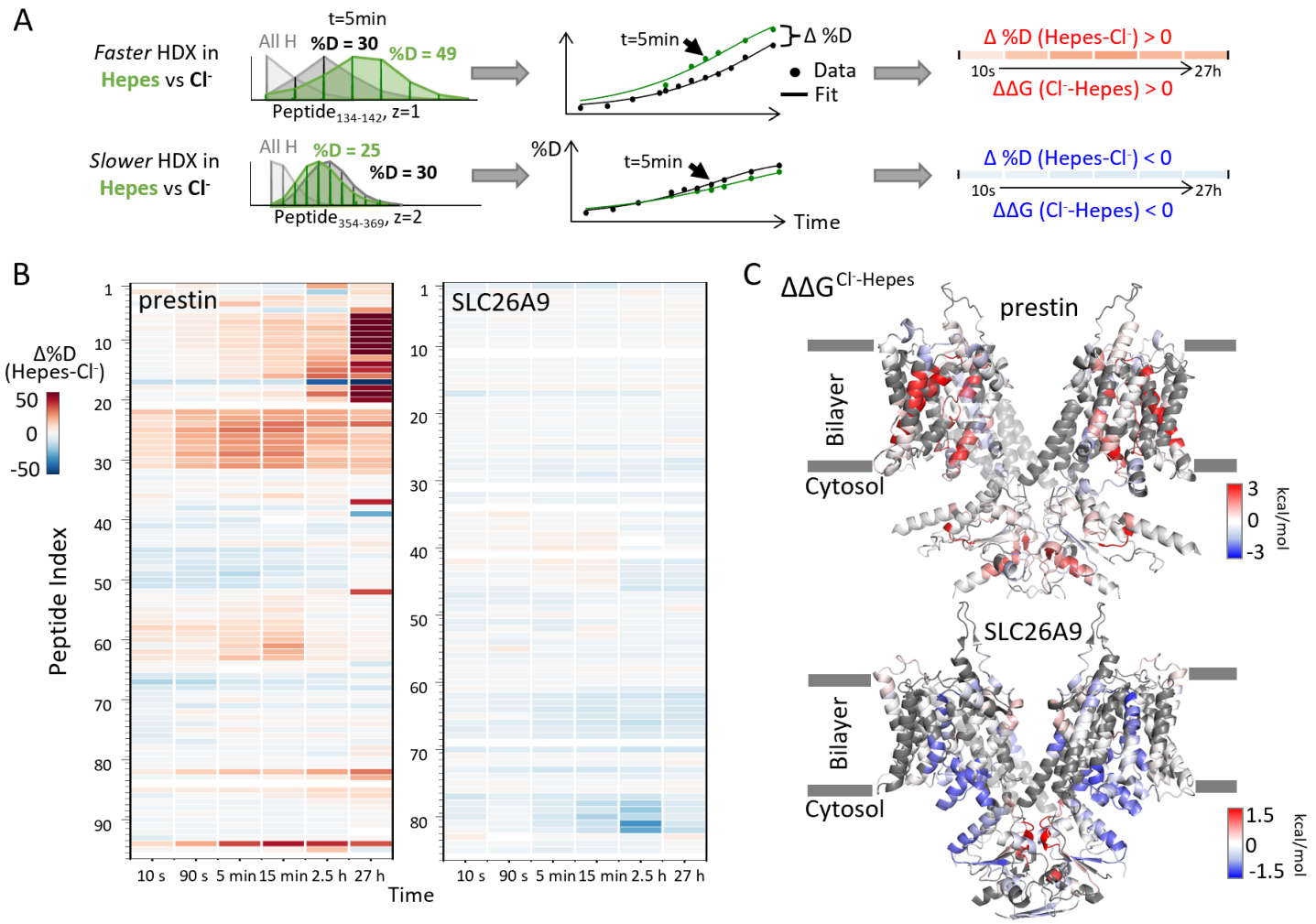

Figure 1: Distinct HDX response of prestin and SLC26A9 to Cl^- binding. (A) HDX data analysis to obtain **(B)** and **(C)**. One example peptide is shown in cases where HDX becomes faster or slower in Hepes (the apo state) compared to in Cl^-. Deuteration levels are obtained from the mass spectra. Here spectra for the undeuterated peptide (grey) and after 5 min HDX labeling in Cl^- (black) and Hepes (green) are shown as an example. The resulting deuterium uptake plots are used to generate the differential deuteration heatmaps in **(B)**. Changes in free energy of unfolding (ΔΔG) in **(C)** are calculated after fitting the data with a stretched exponential (**Methods**)[17]. **(B)** Heatmaps showing the difference in deuteration levels at each labeling time for all TMD peptides of prestin and SLC26A9 measured in Hepes compared to Cl^-. Peptide sequences corresponding to peptide indexes can be found in Fig. S9 & Fig. S10. **(C)** Changes in free energy of unfolding (ΔΔG) in Hepes compared to Cl^- for full-length prestin and SLC26A9 mapped onto the structure (PDB 7S8X and 6RTC). Red and blue indicate increased and decreased stability upon Cl^- binding, respectively. Following regions of the left subunits are shown as low transparency to highlight the binding site – prestin: TM5 and TM12-14; SLC26A9: TM5 and TM13-14. Regions with no fitting results are in grey.

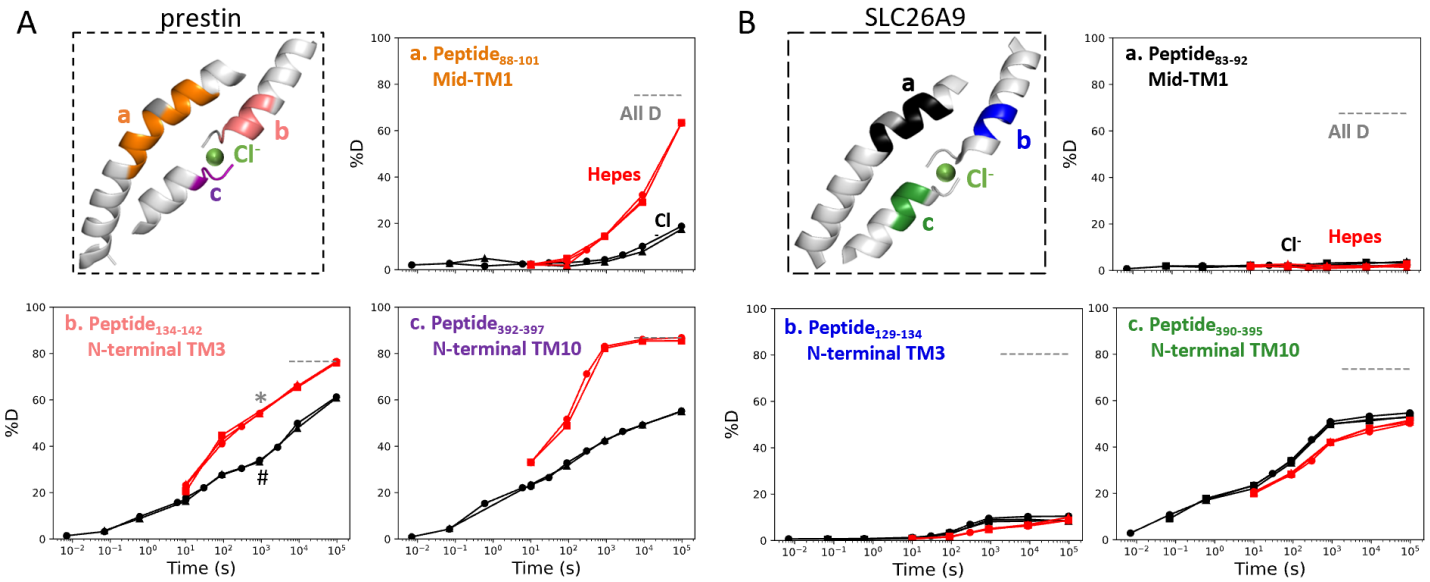

Figure 2: Cl^- binding stabilizes prestin's anion-binding pocket (A) but mildly affects SLC26A9's (B). The structure shows the anion-binding pocket (TM1, TM3, and TM10) with the putative position of the bound Cl^-. Colored regions correspond to peptides whose deuterium uptake plots are shown (prolines are colored in grey) when the protein is in Cl^- (black) and in Hepes (red). Grey dashed lines indicate deuteration levels in the full-D control. Data from two and three biological replicates are shown for prestin in Cl^- and Hepes, respectively. Data from three technical replicates are shown for SLC26A9. Replicates are shown as circles, triangles, and squares. Some replicates are superimposable and hence not observable. The symbols (* and #) in **(A.b)** denote data points used in **Fig. 3B**.

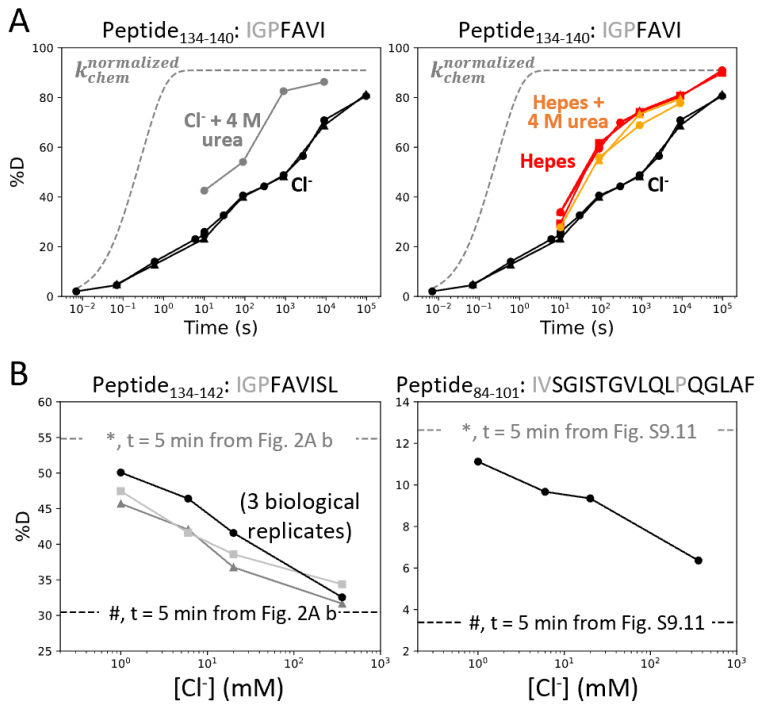

Figure 3: Anion binding folds and stabilizes prestin's binding site. (A) Deuterium uptake plots for the N-terminus of TM3 ($Peptide_{134-140}$) measured in the absence and presence of 4 M urea, in a background of (**Left**) Cl^- and (**Right**) Hepes. Replicates (circles, triangles, and squares): 2 in Cl^-, 3 in Hepes, 2 in Hepes with urea, biological. Grey dashed curves represent deuterium uptake with k_{chem}[34,35], normalized with the back-exchange level. **(B)** Deuteration levels for (**Left**) the N-terminus of TM3 ($Peptide_{134-142}$) in three biological replicates and for (**Right**) TM1 ($Peptide_{84-101}$) after 5 min labeling upon titrating Cl^- to apo state of prestin. Dashed lines indicate deuteration levels at t = 5 min (* and # for apo and Cl^--bound states, respectively) taken from **Fig. 2A.b** and **Fig. S9.11**. Residues in grey denoted in the peptide sequence do not contribute to the deuterium uptake curve.

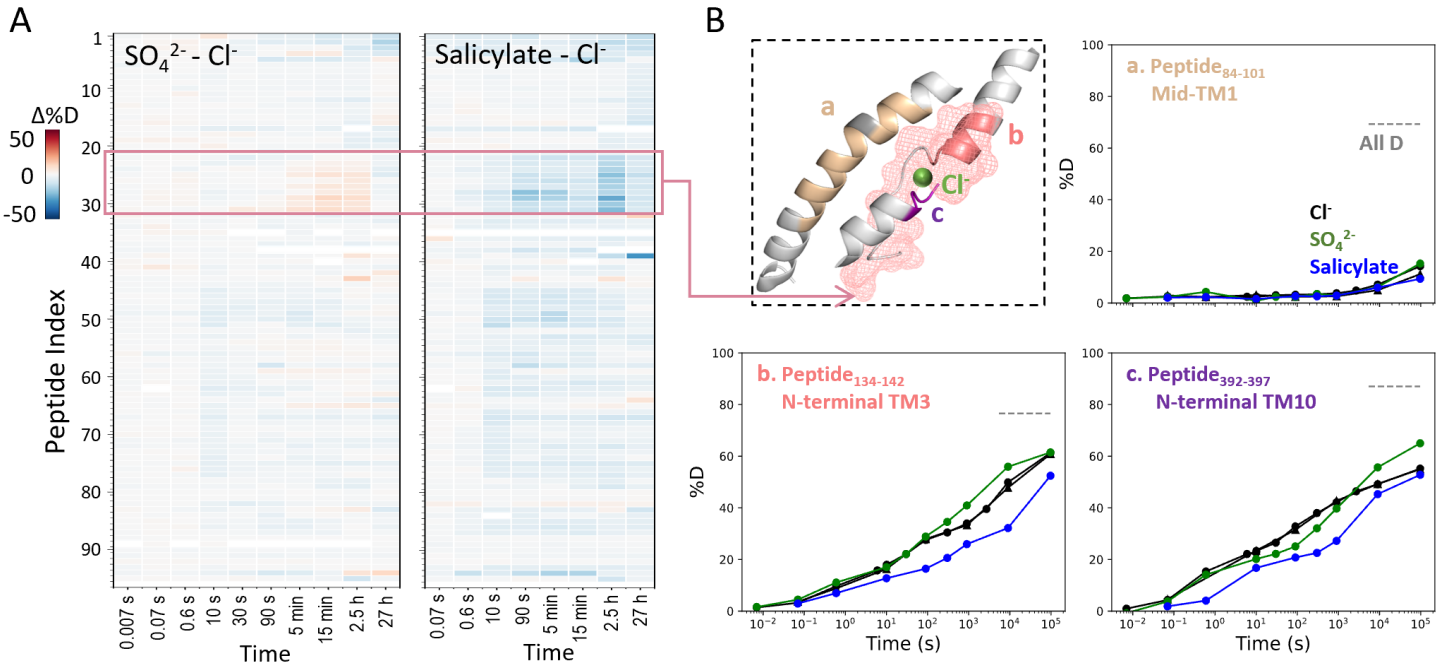

Figure 4: HDX of prestin in various anions (Cl^-, SO_4^{2-}, and salicylate) predominantly differ at the binding site. (A) Heatmaps showing the difference in deuteration levels at each labeling time for all TMD peptides measured in SO_4^{2-} or salicylate compared to Cl^-. Peptide sequences corresponding to peptide indexes can be found in Fig. S9. **(B)** The structure shows the anion-binding pocket with the putative position of the bound Cl^-. The pink mesh highlights the region with the greatest HDX response to anion binding. Colored regions correspond to peptides whose deuterium uptake plots are shown (prolines are colored in grey) when the protein is in Cl^- (black, two biological replicates shown in circles and triangles), SO_4^{2-} (green), and salicylate (blue). Grey dashed lines indicate deuteration levels in the full-D control.

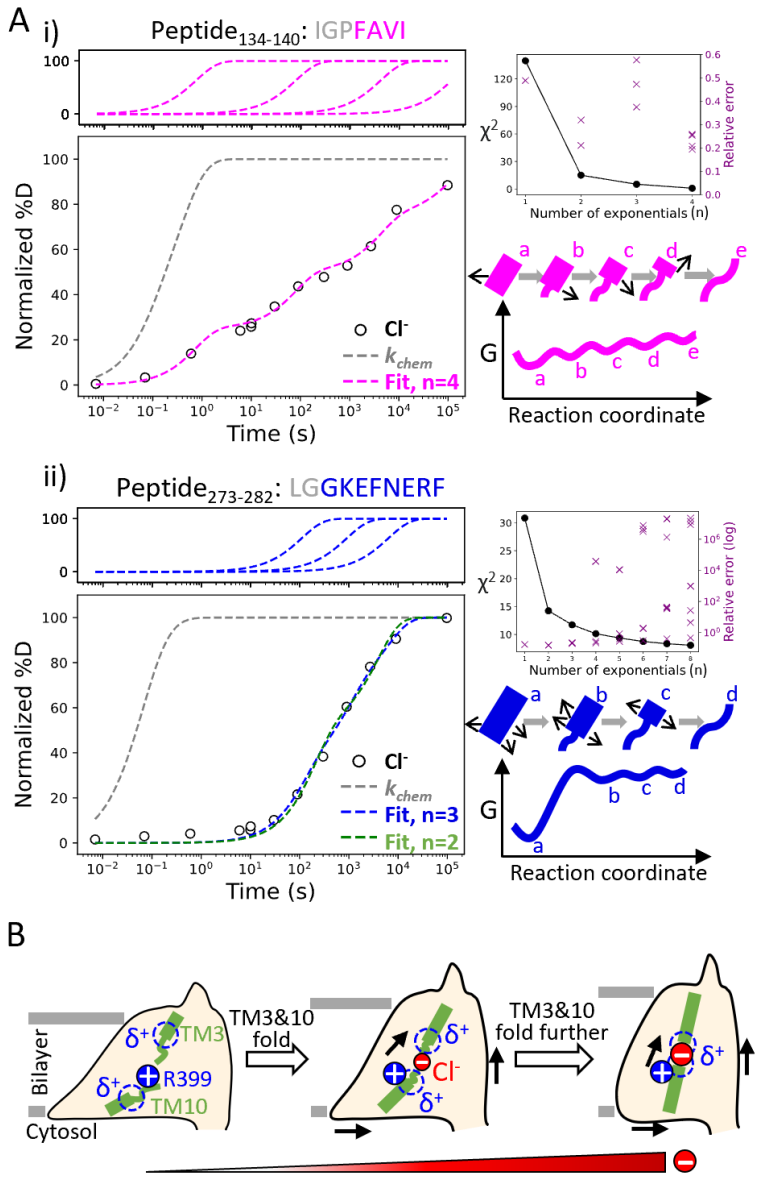

Figure 5: Helix fraying, cooperative unfolding, and the proposed mechanism for prestin's electromotility. (A) Left: Deuterium buildup curves for **(i)** the N-terminal TM3 ($Peptide_{134-140}$) and **(ii)** the intracellular portion of TM6 ($Peptide_{273-282}$) in Cl^- depicting helix fraying and mild cooperativity, respectively. Circles show experimental deuteration levels, normalized with in- and back-exchange levels. Grey dashed curves show hypothetical intrinsic uptake curves (PF = 1). On the top shows individual exponentials whose sum is fitted to the experimental values and plotted on the main buildup curves. Residues in grey denoted in the peptide sequence do not contribute to the deuterium uptake curve. **Upper right:** χ^2 and the relative error as the number of fit exponentials increases, used to assess the quality of fit. **Lower right:** Models and free energy surface of unfolding illustrating the difference between **(i)** fraying and **(ii)** mild cooperativity. **(B)** Mechanism for prestin's conformational transition from the expanded to the contracted state regulated by the anion concentration. Green rectangles and curved lines: folded and unfolded fractions, respectively, of TM3 and TM10. Blue filled circle: R399. Blue dashed circle: partial positive charges from TM3 and TM10 helical dipoles. Red filled circle: anions, with the size of the circle depicting anion concentrations. Black arrows: prestin's conformational change.